


An in-silico proof-of-concept of electrohydrodynamic air amplifier for low-energy airflow generation

Journal Article**Author(s):**

Rubinetti, Donato; Iranshahi, Kamran; [Onwude, Daniel](#) ; Xie, Lei; Nicolaï, Bart; Defraeye, Thijs

Publication date:

2023-04-20

Permanent link:

<https://doi.org/10.3929/ethz-b-000604160>

Rights / license:

[Creative Commons Attribution 4.0 International](#)

Originally published in:

Journal of Cleaner Production 398, <https://doi.org/10.1016/j.jclepro.2023.136531>



An in-silico proof-of-concept of electrohydrodynamic air amplifier for low-energy airflow generation

Donato Rubineti^{a,b}, Kamran Iranshahi^{a,c}, Daniel I. Onwude^a, Lei Xie^d, Bart Nicolai^b, Thijs Defraeye^{a,*}

^a Empa, Swiss Federal Laboratories for Materials Science and Technology, Laboratory for Biomimetic Membranes and Textiles, Lerchenfeldstrasse 5, CH-9014, St. Gallen, Switzerland

^b KU Leuven, BIOSYST-MeBioS, Willem de Croylaan 42, Heverlee, Belgium

^c ETH-Zurich, Swiss Federal Institute of Technology, Zurich, 8092, Switzerland

^d Belimed AG, Grienbachstrasse 11, CH-6300, Zug, Switzerland

ARTICLE INFO

Handling Editor: Jin-Kuk Kim

Keywords:

Air propulsion

CFD

Electrohydrodynamics

Corona discharge

Ionic wind

Coanda effect

ABSTRACT

Electrohydrodynamic (EHD) technology generates airflow without moving parts, making it a reliable solution for various low-energy applications. EHD-based airflow devices enhance airflow patterns, resulting in significant energy savings in air-moving systems. This airflow, also known as ionic wind, is created through Corona discharge, which accelerates electrically charged air molecules in a strong electric field. Currently, EHD's low electrical-to-mechanical energy conversion rate still limit its ability to generate large flow rates. The objective of this study is to enhance the flow rate of EHD-based devices, for applications where EHD can be used as an effective auxiliary technology with low pressure lift, to enhance airflow distribution and circulation. To this end, a novel bladeless air propulsion device is proposed that combines ionic wind with air amplification based on the Coanda phenomenon to amplify EHD-generated flow rates. We assess the performance of the bladeless air propulsion device to generate airflow by investigating fluid dynamics, electrostatics, and energy consumption. We demonstrate the proof-of-concept with an innovative fully-coupled simulation approach for corona discharge and EHD modeling. We explore different design parameters on the conceptual EHD air amplifier, such as the electric potential (10–30 kV) of the discharge electrode, the electrode spacing (5–25 mm), and the channel height (30–150 mm). The studies are performed on a 2D constrained channel flow and a 2D-axisymmetric open space design, respectively. In order to quantify the benefit of air amplification on EHD, the results are benchmarked to a regular EHD setup without amplifying vane as well as to a comparable commercial axial fan. We assess the performance in terms of flow rate per electric power input. Here, the EHD air amplifier in the constrained flow configuration increases the total flow rate by 59% compared to regular EHD and 48% compared to the axial fan for the same electrical energy input. Amplification factors of 16.5–19 are achieved for the constrained configuration and 5.5 to 6.4 for the open space configuration. The predicted energy consumption is 4–17.5 W for the open space configuration, resulting in flow rates up to 140 m³ h⁻¹. These results show that EHD air amplification is a promising way to generate high flow rates with low pressure rise at a low electrical cost, by which it can provide a more sustainable alternative to conventional fans in specific applications.

1. Introduction

Fans are common components in many everyday systems, from small electronic devices to HVAC (heating, ventilation, air conditioning) systems. These systems are used to move air, but in some cases consume a large amount of energy. For instance, in developed countries, HVAC systems account for 20% of the total energy consumption (Chua et al.,

2013). To achieve energy savings, a sustainable approach is to improve air distribution and circulation through low-cost measures that effectively guide airflow to the target area (Zhang and Li, 2020), (Shao et al., 2022). In addition, conventional air-moving devices, with their centralized rotor-blade arrangements, still require airflow guides to distribute the airflow towards the target area, which can be significantly larger than the fan diameter (Ambaw et al., 2014). With conventional air propulsion technologies, only incremental optimizations are likely to

* Corresponding author.

E-mail address: thijs.defraeye@empa.ch (T. Defraeye).

<https://doi.org/10.1016/j.jclepro.2023.136531>

Received 28 June 2022; Received in revised form 19 January 2023; Accepted 19 February 2023

Available online 21 February 2023

0959-6526/© 2023 The Authors. Published by Elsevier Ltd. This is an open access article under the CC BY license (<http://creativecommons.org/licenses/by/4.0/>).

List of symbols*Symbol Meaning SI Unit*

AF	Amplification factor	\dot{V}	Volume flow rate, $\text{m}^3 \text{s}^{-1}$
b	Ion mobility, $\text{m}^2 \text{V}^{-1} \text{s}^{-1}$	\dot{V}_{in}	Inlet volume flow rate, $\text{m}^3 \text{s}^{-1}$
D	Inner diameter, m	\dot{V}_{out}	Outlet volume flow rate, $\text{m}^3 \text{s}^{-1}$
D_{ion}	Ion diffusivity, $\text{m}^2 \text{s}^{-1}$	W	Width of the channel, m
D_0	Electric displacement vector, C m^{-2}	y^+	Dimensionless wall distance,
E	Electric field vector, V m^{-1}	γ	Flow rate per electrical power, $\text{m}^3 \text{h}^{-1} \text{W}^{-1}$
E_0	Corona discharge onset field strength, V m^{-1}	δ	Emitter-collector distance, m
E_e	Corona discharge onset field strength on electrode, V m^{-1}	ε	Vane nozzle gap, m
F_q	Coulomb force, N	ε_0	Vacuum permittivity, F m^{-1}
H	Channel height, m	ε_r	Relative permittivity, F m^{-1}
I	Electric current, A	μ	Dynamic viscosity of air, Pa s
J	Current density, A m^{-2}	ϕ	Electric potential, V
P_{el}	Electric power, W	ϕ_1	Electric potential on emitter electrode, V
p	Pressure, Pa	ρ	Density of air, kg m^{-3}
r_e	Emitter electrode curvature, m	ρ_{el}	Space charge density, C m^{-3}
u	Velocity field vector, m s^{-1}	$\rho_{el,0}$	Initial space charge density on electrode, C m^{-3}
\bar{u}	Average velocity, m s^{-1}	Ω	Computational domain, m^2
		Ω_{PLA}	Computational subdomain for PLA enclosure, m^2
		Ω_{air}	Computational subdomain of air, m^2

occur in the future to make ventilation more sustainable. For more disruptive steps forward, new technologies need to be deployed.

One example of such a technology is electrohydrodynamic (EHD) drying (Iranshahi et al., 2020), (Taghian Dinani and Havet, 2015). EHD drying uses a locally produced airstream and eliminates energy-intensive heating elements with enhanced airflow circulation, resulting in energy savings and reduction of greenhouse gas emissions. Electrohydrodynamics technology allows for precise manipulation of airflow, enabling the creation of decentralized airflow and the enhancement of existing technologies. However, as a standalone technology, EHD, also known as ionic wind, has limitations, such as a limited pressure rise (Jewell-Larsen et al., 2011). EHD is particularly promising for applications where it is important we have operation without moving parts and generation of vibration-free and silent airflow. This technology requires minimal components to generate airflow.

EHD airflow is created by a corona discharge between two or more electrodes when a high voltage is applied. Corona discharge is a plasma zone that forms when the fluid, such as air around a conductor, is ionized (Iranshahi et al., 2020). In an electric field, the charged air molecules accelerate under the influence of the Coulomb force and transfer momentum to the surrounding neutral air by collision. As a result, a macroscopic airflow emerges. This airflow can be achieved solely by choosing a suitable electrode arrangement and a high voltage cable connecting the electrodes to a power source. The fundamentals of EHD airflow generation are well-known. However, air propulsion technology has rarely considered the ionic wind principle as a viable alternative to common fans, mainly because of the limited pressure rise EHD can overcome. However, EHD has the potential to be a cleaner production method as the discharge process itself is very energy-efficient (Iranshahi et al., 2020) and the design of EHD is focused on creating thrust rather than pressure rise.

Many different EHD enhancement techniques have been investigated. Impressive airflow velocity gains were obtained via the optimization of electrode arrangement (Tirumala and Go, 2011), (Johnson et al., 2015), a surface-enlarging nanomaterial coating of discharging electrodes (Wu et al., 2017), an array design of multiple 3D-printed individual EHD pumps (Kanazawa et al., 2021) or via sequentially connected ionic wind blowers (Rickard et al., 2006). The optimization attempts predominantly target the EHD phenomenon's electrostatic part by studying various types of emitter and collector configurations (Zhang and Yang, 2021). Another approach intends to employ magnetic fields on top of electric fields to augment the acceleration with the Lorentz

force (Wang et al., 2021), (Zhou et al., 2018). However, these studies did not achieve sufficient flow rates to consider EHD as a viable airflow generation technology. To fill this gap, we focus on improving efficient EHD-driven airflow by aerodynamic effects instead of improving the generation of higher flow rates on the electrostatic end alone.

For this purpose, we numerically investigate the combination of EHD with the principle of air amplification using the Coanda effect. The Coanda effect is the tendency of a fluid flow to stay attached to a solid wall, preferably convex, and remain attached even when the guiding wall deviates from the initial flow direction due to pressure asymmetries (Panitz and Wasan, 1972), (Dumitrache et al., 2012). This principle can be used to amplify airflow rates by entrainment of the surrounding air. In practice, an EHD-generated airstream jet is directed towards a solid wall, and a priori stagnant surrounding air volume accelerates as well. The accelerated air volume is driven by a pressure difference and requires no other air propulsion device, leading to an overall flow rate and transduction efficiency increase. We demonstrate a geometry featuring EHD and the Coanda effect in a 2D confined channel and a 2D-axisymmetric variant for the free flow case for the in-silico proof-of-concept. Because of the multiphysical nature of EHD and the complexity of combining it with airflow amplification using the Coanda effect phenomenon, we developed an advanced single-species modeling approach. This approach iteratively adjusts the initial space charge density on the emitting electrode. The advancement is employed via a Lagrange multiplier as the fitting parameter that satisfies the Peek-Kaptzov condition.

2. Materials and methods

This simulation strategy studies the EHD air amplification influence parameters of the vast design space, such as wire radius, electrode spacing, operation voltage, channel height, and vane slit size. The results of EHD air amplification are compared to regular EHD and a standard fan in terms of flow rate, power consumption, and flow rate to electrical power ratio to benchmark the transduction efficiency gain of combining EHD airflow with the Coanda effect. The simulation study is performed first on a constrained flow $150 \times 150 \times 500 \text{ mm}^3$ channel simplified to a 2D domain with a wire-type electrode. Then, a 2D-axisymmetric case for open space EHD air amplification is accordingly investigated and compared.

All simulations are performed using a two-dimensional (2D) and two-dimensional axisymmetric (2Da) model. The model accounts for

electrostatics (corona discharge) and turbulent airflow (CFD) and is fully coupled. The discharge phenomenon is considered via a single-species approach within the air domain. This way, the ionized and charge-free air fractions are both represented as a continuum, with the space charge density being the relevant distinction variable. The details for boundary conditions, assumptions, and simulation parameters are highlighted in this section.

2.1. Couplings in electrohydrodynamic airflow

EHD airflow is a complex multiphysical process that couples electrostatics and fluid flow. Ions are produced by the emitter electrode and accelerated via Coulomb force in the drift region. In transition from the emitter electrode to the collector electrode, the ions collide with air molecules, thus, generating a macroscopic airflow. The electrostatic action is influenced by geometrical factors and inherent physical conditions, such as the minimum electric field intensity around the emitter to initiate ionization which is called corona onset field strength. Fig. 1 maps the most relevant couplings and influence factors involved in EHD airflow generation.

EHD airflow itself is the consequence of the Coulomb force, which arises as a product of the electric field and space charge distribution. These two are highly influenced by several design parameters, such as emitter electrode curvature, applied voltage on that electrode, and emitter-collector arrangement. Moreover, the electric field and space charge density interact by mutually influencing each other's distributions and intensities by charge migration and field distortion. As far as the electrostatic part of the problem is concerned, the emitter-collector arrangement, electrode shape, and the applied voltage are crucial design and tuning parameters.

2.2. EHD air amplification as a combination of regular EHD with the Coanda effect

Linking EHD airflow with the Coanda effect results in EHD air amplification. In the first step, a regular EHD airstream is generated as by-product of corona discharge between two electrodes. This primary airstream is directed towards a nozzle or inlet and expanded on a nearby solid wall. The shape of the wall can be flat or convex. Due to one-sided pressure differences around the nozzle, the primary airstream is forced to remain attached to the solid wall. This causes the surrounding air to accelerate as well, thus, inducing a secondary airstream via air entrainment. The overall result is that the primary airstream is amplified without additional energy cost by means of the aerodynamic perks offered by the Coanda surface. The Coanda surface is the solid wall capable of expanding and attaching the primary airstream. Figs. 3 and 4 show principle sketches of EHD air amplification.

2.3. Geometrical configurations

Three different geometrical configurations are investigated based on induced physics. The first is a regular EHD channel setup (#1) without air amplification that serves as a benchmark. The second configuration (#2) is EHD with air amplification in a channel to investigate the principle and added value compared to regular EHD. Finally, an open space EHD air amplifier configuration (#3) is constructed to investigate whether flow confinement (in a channel) reduces the entrained flow by the Coanda effect. Commercially available fans employing air amplifier technology inspired the design of the amplifying geometries (Gammack et al., 2012). Irrespective of the enclosure shape, three components must always be present for EHD air amplification: (1) a high voltage electrode, either a wire or a needle, or any other suitable sharp and strongly curved entity, (2) an enclosure where the electrodes are placed and a (3) Coanda surface. The enclosure is physically relevant to produce an EHD airstream separately and also to protect the outer environment from

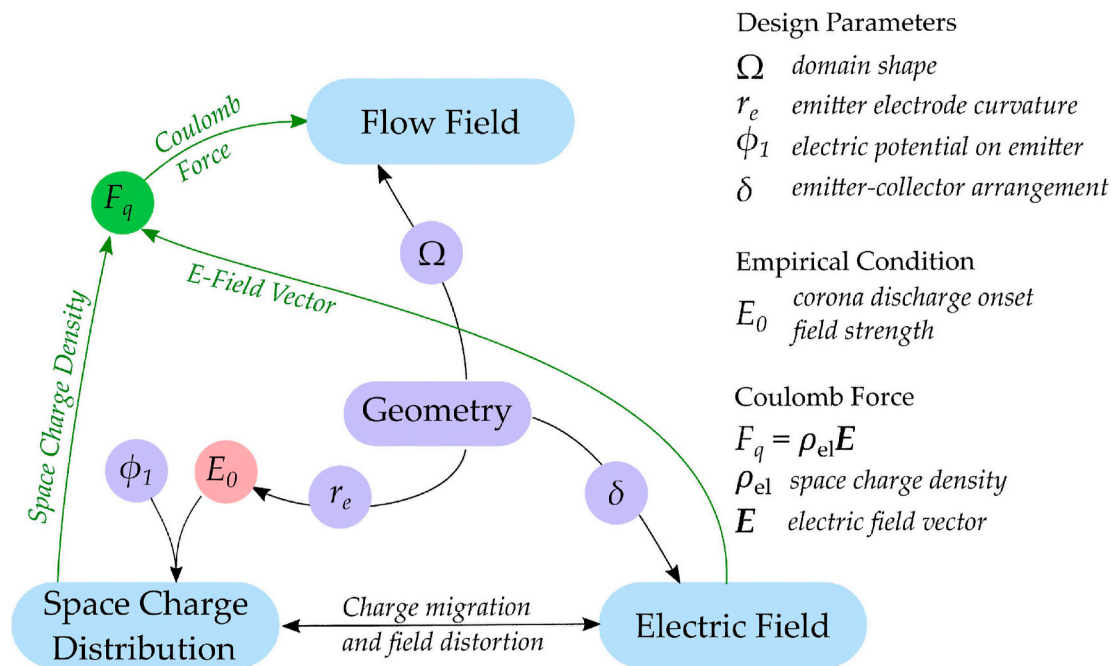


Fig. 1. EHD airflow is a complex multiphysical phenomenon where the flow field establishes as a consequence of interactions between the space charge distribution and electric field. The geometry of the system provides the design parameters (purple), which highly influence all dependent fields (light blue; flow field, electric field, space charge distribution). Moreover, the production of charge is dependent on the onset field strength, an empirical condition (pink). From the electrostatic fields (space charge density and electric field), we obtain the Coulomb force, acting as body force onto the fluid and creating, as a consequence, a macroscopic airflow. This is a simplified representation of the multiphysical couplings and the design space of EHD airflow, which poses the basis for EHD air amplification. (For interpretation of the references to colour in this figure legend, the reader is referred to the Web version of this article.)

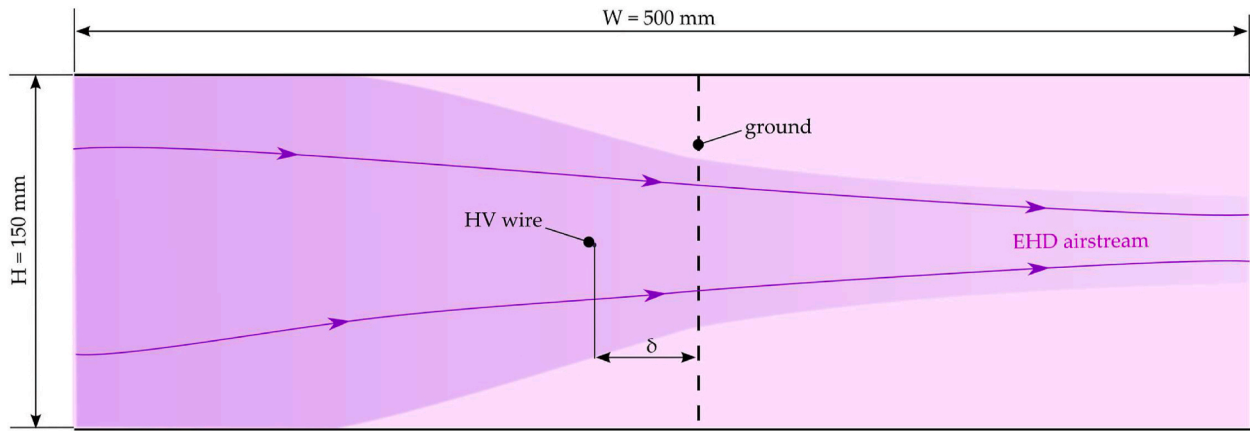


Fig. 2. The confined space configuration #1 of regular EHD without air amplification serves as benchmark. It includes a high voltage (HV) wire as emitter and a ground collector. The emitter-collector distance δ is variable.

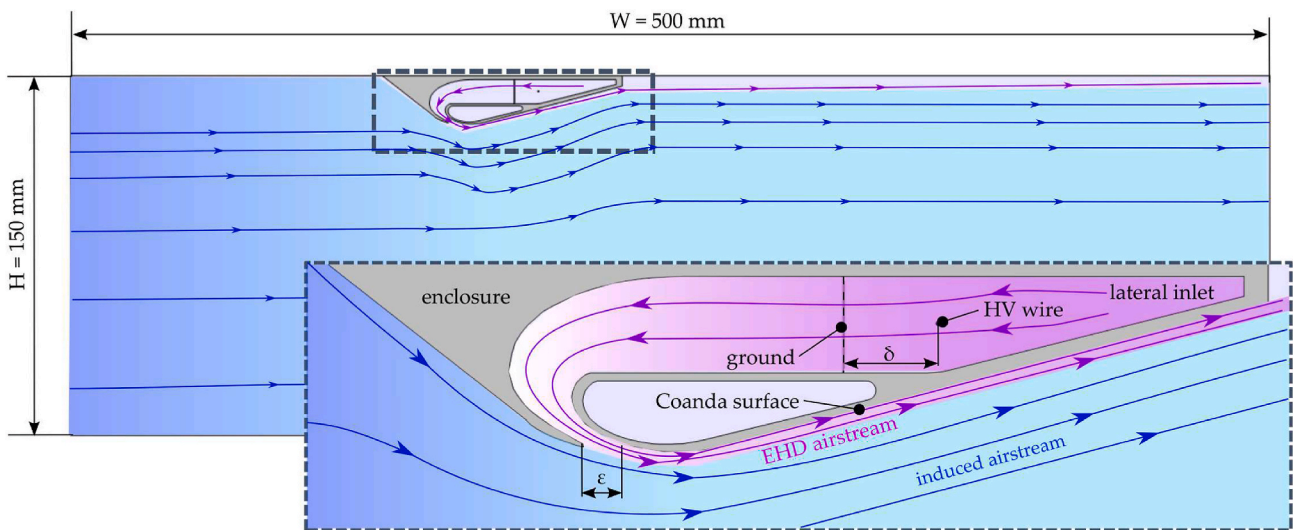


Fig. 3. The confined space configuration #2 of EHD air amplification features an enclosure (or vane) that accommodates the electrical components. Within the enclosure, a high voltage wire and ground act as accelerators of a primary airstream, e.g., the EHD airstream. This EHD airstream is pushed through a nozzle with gap size ϵ and remains attached to an inclined Coanda surface. As a result, a larger airflow is induced, which ultimately leads to the amplification of airflow rates.

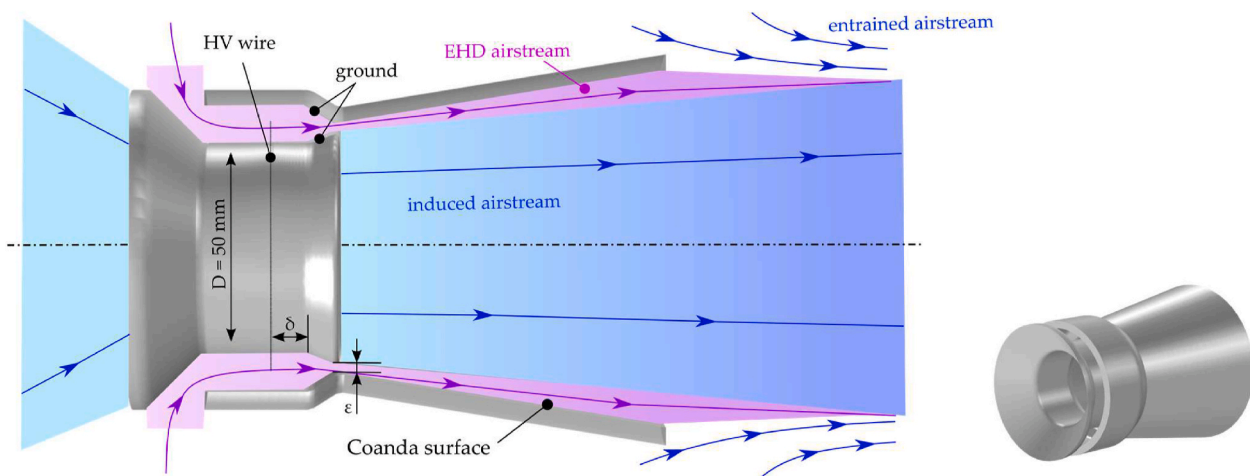


Fig. 4. The open-space configuration #3 of EHD air amplification is a 2D-axisymmetric geometry where the electrical components are embedded in the overlapping region of two separate pieces. Within the overlapping region, the primary stream (EHD airstream) is generated and pushed through the nozzle with gap size ϵ . As the EHD airstream remains attached to the Coanda surface, it also induces an airstream in the inner volume. Due to the open space configuration, another airstream is accelerated, the entrained airstream, which further increases the flow rate.

high voltage (HV) components.

2.3.1. Confined space regular EHD configuration (#1, benchmark)

This simple 2D configuration serves as a benchmark where the electrode is placed within the confined space, and the corresponding ground varies in distance, as seen in Fig. 2. No air amplification occurs here, as the EHD-generated airflow itself is the main bulk flow within the channel.

2.3.2. EHD air amplification configuration in a confined space (#2)

This 2D configuration features an enclosure, also termed “vane,” where the electrodes are placed inside, generating an EHD airstream, as shown in Fig. 3. Within the vane, a wire electrode with a radius r_e , which is used to start the corona discharge process and a grounded mesh electrode with a porosity of 70% is employed. A porosity of 70% corresponds to a mesh structure with a 1 mm wire diameter and 6 mm pitch. The spacing between wire and ground is δ . The EHD-generated airstream is pushed through a slit with a gap size ε and is expected to remain attached to the Coanda surface. As a result, the Coanda effect is invoked, which drags the air of the channel leading to an amplified airstream.

2.3.3. EHD air amplification configuration in open space (#3)

The third configuration is a 2D-axisymmetric geometry in an open space. Here, we test the performance of EHD air amplification in an open room with a circular enclosure of inner diameter D . Like in the previous case, this configuration features the main components needed for EHD air amplification, i.e., electrodes, enclosure, and Coanda surface. The electrode, in this case, is again a wire which is circularly arranged within the enclosure with a spacing from the ground (δ). The corresponding ground counterpart is built into the slit with a gap distance ε .

2.4. Physics-based continuum model

In order to run the specified calculations, a fully coupled corona discharge computational fluid dynamics (CFD) flow model is developed, which lowers the computational cost. Hence, three governing equations are calculated in a single study step. However, current single-species EHD numerical models, where the ionized fraction of air is described by the continuum variable space charge density, rely on a multi-step approach involving guessing the initial space charge on the emitting electrode (Kasdi, 2019; Defraeye and Martynenko, 2018a; Onwude et al., 2021). Indeed, physics-based modeling of EHD is a complex endeavor due to the a priori unknown initial space charge generated on the corona discharge wire at a given voltage. This section discusses the governing equations used for the coupled EHD and airflow and proposes a novel approach to dynamically compute the initial space charge within the solver loop by adding a Lagrange multiplier as correcting variable.

2.4.1. Corona discharge model

The corona discharge part of the EHD model features Poisson’s equation (Eq. (1)) with the electric potential ϕ [V] as the dependent variable and the charge convection model with the space charge density ρ_{el} [C m⁻³] as the dependent variable. The first governing equation writes

$$\nabla^2 \phi = -\frac{\rho_{el}}{\varepsilon_0 \varepsilon_r} \quad (1)$$

with ε_0 the vacuum permittivity (in air, $\varepsilon_r = 1$). The second governing equation is the conservation of charge, i.e., the continuity equation for current density, J [A m⁻²],

$$\nabla \bullet J = 0 \quad (2)$$

Conveniently, we can express the current density J in terms of Ohm’s law and by defining the electric field as $E = -\nabla \phi$

$$J = \rho_{el} b E + \rho_{el} u - D_{ion} \nabla \rho_{el} \quad (3)$$

Here, b stands for the ion mobility (in air, $1.8 \times 10^{-4} \text{ m}^2 \text{ V}^{-1} \text{ s}^{-1}$), u [m s⁻¹] is external convection and D_{ion} [m² s⁻¹] is the ion diffusivity. Often, the diffusive ($D_{ion} \nabla \rho_{el}$) and external convection terms ($\rho_{el} u$) are neglected due to the dominance of up to two orders of magnitude of the electrical field-based ion shift term in Equation (3) (Iranshahi et al., 2020), (Guan et al., 2018). Nevertheless, we also note that the diffusive term may prove useful to improve numerical stability. Furthermore, the electric field vector E can be expressed as the negative gradient of the electric potential. Hence, the corona discharge model is fully described by Equations (1)–(3) with two dependent variables, ϕ and ρ_{el} , requiring at least two boundary conditions for the electric potential and one boundary condition for the space charge density.

The boundary condition for the initial space charge requested by Equation (2) is of the Dirichlet type, and a priori unknown for single-species modeling approaches. While it is possible to find its value iteratively, it remains a tedious and time-consuming procedure that needs to be repeated for each electric potential value. Moreover, a single initial space charge value on the electrode can produce errors as the value is not necessarily constant over the entire boundary, as detailed in Supplementary Material C. Employing a constant initial space charge density on the electrode is error-prone.

We avoid such numerical errors by retrieving the information for the initial space charge $\rho_{el,0}$ directly from Poisson’s equation. Here, instead of specifying the given electric potential ϕ_1 on the wire, we enforce a weak constraint on the electrode boundary.

$$0 = (\phi_1 - \phi). \quad (4)$$

For practical implementation, Equation (4) is defined by test functions or any other suitable optimization method. We chose the Lagrange multiplier approach, where the constraint is enforced by introducing another dependent variable, λ , within the solver loop. Conveniently, the newly introduced Lagrange multiplier variable is the initial space charge density $\lambda = \rho_{el,0}$, which can then be inserted into Equation (2). The boundary condition for the grounded electrode remains unchanged and is of Dirichlet type, i.e. $\phi_1 = 0$ V.

Information about the electric field on the boundary is needed as well. We retrieve the information via an electric displacement boundary condition

$$D_0 = [0 - \varepsilon_0 E_e]^T \quad (5)$$

The electric displacement vector D_0 is parallel to the normal boundary vector. E_e is the empirically defined electric field strength on the surface of the electrode

$$E_e = E_0 \left(1 + \frac{2.62 \times 10^{-2}}{\sqrt{r_e}} \right) \quad (6)$$

with $E_0 = 3.31 \times 10^6$ [V m⁻¹] being the ionization breakdown electric field strength in air at standard conditions for a smooth electrode (Jewell-Larsen et al., 2008). This is the generally accepted breakdown condition to invoke corona discharge, also known as the Peek-Kaptzov assumption (Ramadhan et al., 2017). With Equation (6), we complete the description of the fully automatized corona discharge modeling approach. The critical point of this coherent formulation is to replace the electric potential on the discharge electrode with a weak formulation of the electric potential and simultaneously include information about the required electric field on the same boundary. We need to match the electric potential weak constraint and the electric field condition. Thus, we introduce another fitting parameter as the Lagrange multiplier, which can then be deployed as the boundary condition for the initial space charge into the charge transport equation. This way, we enable the efficient calculation of extensive parametric studies by avoiding the iterative determination of the space-charge density boundary condition.

2.4.2. Turbulent airflow computational fluid dynamics (CFD) model

The Navier-Stokes momentum equation describes the airflow part of EHD air amplification with an additional source term for the Coulomb force F_q [N].

$$\rho \mathbf{u} \bullet \nabla \mathbf{u} = -\nabla p + \mu \nabla^2 \mathbf{u} + \mathbf{F}_q \quad (7)$$

$$\mathbf{F}_q = \rho_{el} \mathbf{E} \quad (8)$$

Here, ρ is the air density [kg m^{-3}], \mathbf{u} is the velocity field [m s^{-1}], p is the pressure [Pa], and μ is the dynamic viscosity [Pa s]. Via the Coulomb force, the airflow model couples to the corona discharge model for the full EHD model.

We adopt a Reynolds-averaged Navier Stokes (RANS) approach in the airflow model. The standard $k-\epsilon$ turbulence model is chosen to represent non-laminar behavior in CFD. We found that $k-\epsilon$ with a turbulence intensity of 5% provides the best stability to scan the vast design space and perform comparative studies. Several other models were tested, e.g., $k-\omega$, SST, $v2f$ with and without wall functions. The turbulence model study and justification for the turbulence model choice are detailed in [Supplementary Material D \(Diffuser, 2023\)](#). In the studies, the mesh adjacent to walls was sufficiently refined in order to obtain values of about 1 for the dimensionless wall distance y^+ . At such small y^+ , the viscous sublayer of wall-bounded flows is resolved at a high confidence level. We observed that the $k-\epsilon$ turbulence model in combination with wall functions and a boundary layer mesh size respecting $y^+ \approx 1$ gives satisfactory precision in representing the Coanda effect in our configurations. The turbulence model could be further finetuned, but this is beyond the scope of this study.

2.4.3. Boundary conditions

[Fig. 5](#) and [Table 1](#) summarize the necessary boundary conditions for EHD calculations with the above-described Lagrange multiplier approach. Note that the boundary conditions are given for the constrained EHD air amplification configuration #2. For the benchmark case, the conditions are the same except for the vane inlet that is not applicable, and the channel inlet becomes an inlet with total pressure $p_{tot} = 0$ Pa instead of an opening. For the open space EHD air amplification configuration #3, the air domain is much larger and has an opening with 0 static pressure.

For EHD air amplification cases, the computational region consists of two domains, an air domain Ω_{air} and a polylactic acid (PLA) domain Ω_{PLA} with an assumed relative permittivity of $\epsilon_r = 3$ ([Behzadnezhad et al., 2018](#)). PLA is chosen as the material for the enclosure due to its widespread use in additive manufacturing. An enclosure of such geometric complexity is ideally manufactured in a 3D-printed way to continue our research on EHD air amplification experimentally. Within the air domain, a density $\rho = 1.2 \text{ kg m}^{-3}$, dynamic viscosity $\mu = 1.81 \cdot 10^{-5} \text{ Pa s}$ and a relative permittivity of $\epsilon_r = 1$ are assumed.

Table 1

Boundary conditions overview for configuration #2.

Boundary	Poisson Equation (1)	Charge Transport (2), (3)	Airflow (7)
Channel inlet	Zero charge	Zero flux	Opening, $p = 0$ Pa
Channel outlet	Zero charge	Zero flux	Opening, $p = 0$ Pa
Vane inlet	Zero charge	Zero flux	Inlet, $p_{tot} = 0$ Pa
Mesh electrode	$\phi = 0$ V	Zero flux	Wire mesh 30% solidity (damping screen)
Wire electrode	$D_0 = [0 - \epsilon_0 E_0]^T$ and $(\phi_1 - \phi) = 0$	$\rho_{el} = \rho_{el0}$	No-slip wall
Elsewhere	Zero Charge	Zero flux	No-slip wall

2.5. Simulation runs

We explore the parameters in the design space of EHD air amplification with the confined space and open space EHD air amplification configurations (#2, #3), while the regular EHD configuration (#1) serves as a reference point. Prior to the parametric studies, a validation case is run on a different geometry for experimental data provided by Jewell-Larsen ([Jewell-Larsen et al., 2008](#)). As preparatory simulation work, a turbulence model study is conducted to choose the best turbulence model for representing the Coanda effect. The results of the turbulence model study are detailed in [Supplementary Material D](#). Additionally, a fluid flow-only case is calculated for the confined space configuration #2, where a standard velocity inlet replaces EHD within the vane to test the aerodynamical operation range of the proposed geometry. The complete set of simulation runs with varying parameters is given in [Table 2](#). The open-space simulation $OSC_{diameter}$ is also a parametric study where only the inner diameter of the construction varies from 10 to 100 mm. In practice, a real EHD device with a gap of $\delta = 5$ mm and a voltage of $\phi_1 = 30$ kV (e.g., CSA_deltaPhi) would likely produce an electrical arc. The arching effect is not modeled in these simulations. The best performing set of parameters for the confined space configuration #2 is ultimately implemented into a separate simulation study ($Csa_orifice$) where the flow is artificially choked via an interior boundary with variable porosity (0–100%) to obtain the EHD air amplifier fan pressure curve.

2.6. Model implementation into numerical simulations

We implement the physics-based EHD model in COMSOL Multiphysics version 5.6, a commercially available finite element software. Corona discharge and airflow physics are solved in one fully coupled solver study. The COMSOL physics modules are “Electrostatics,” “Coefficient Form PDE,” and “Turbulent Flow, $k-\epsilon$.” The parameters are

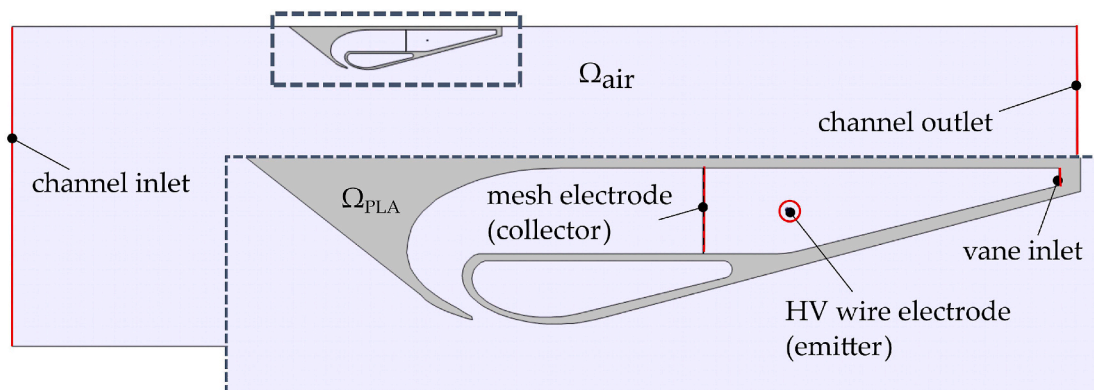


Fig. 5. Configuration #2 with highlighted boundaries. The non-highlighted boundaries are no-slip walls.

Table 2
Simulation list of computational configurations and parameter settings.

Name	Type	Description/Configuration	Wire radius r_e [μm]	Electrode spacing δ [mm]	Voltage ϕ_1 [kV]	Channel height H [mm]	Vane slit ε [mm]
CS0_validation	parametric	validation case (Jewell-Larsen et al., 2008), (Ramadhan et al., 2017)	50	9	5–8	15	n/a
CS0_coanda	parametric	turbulence model study	n/a	n/a	n/a	100	2
CSa_basecase	basecase	confined: amplifying (#2)	250	10	15	150	4
CSa_deltaPhi	parametric	confined: amplifying (#2)	250	5–25	10–30	150	4
CSa_wire	parametric	confined: amplifying (#2)	50–300	10	15	150	4
CSa_slit	parametric	confined: amplifying (#2)	250	10	15	150	1–10
CSa_height	parametric	confined: amplifying (#2)	250	10	15	50–150	4
CSa_onlyFlow	parametric	confined: amplifying (#2)	n/a	n/a	n/a	150	4
CSa_orifice	parametric	confined: amplifying (#2)	250	5	30	150	6
CSb_basecase	basecase	confined: non-amplifying (#1)	250	10	15	150	n/a
CSb_deltaPhi	parametric	confined: non-amplifying (#1)	250	5–25	10–30	150	n/a
OSc_diameter	parametric	open space: amplifying (#3)	50	10	30	n/a	4

varied using parametric sweeps for the simulations in Table 2. The chosen solver is a fully-coupled direct solver, MUMPS (Multifrontal Massively Parallel sparse direct Solver), combined with linear shape functions. For CFD, we adopt a PARDISO (PARALLEL Direct sparse Solver) segregated solver with quadratic shape functions. For parametric studies, the solver was instructed to store NaN (Not-a-Number) solutions to track the feasibility of the design space parameter combinations. Moreover, the maximum number of iterations was set at 500 for every single sweep.

A mesh sensitivity analysis was performed on three separate grids (coarse, medium, fine) with 14 192, 28 029, and 56 050 elements. Via Richardson extrapolation, we found that the coarse mesh differs from the exact solution by a relative error of <2%. Hence, the simulations listed in Table 2 are performed on the coarse mesh. The computational grid is semi-automatically defined with the built-in mesher tool. It comprises mixed elements with strategic refinements in regions of interest or where steep gradients are expected, i.e., on the electrode boundary.

2.7. Metrics to evaluate the performance of EHD air amplifier

We evaluate the EHD air amplifier performance based on a few metrics, namely, the electric current, electric power, airflow rates, and the flow-to-power ratio (transduction efficiency). The electric current I [A] is calculated directly via a boundary integral of the current density of the emitting wire

$$I = H \bullet \int_0^{2\pi r_e} \rho_{el} b \mathbf{E} ds \quad (9)$$

where H [m], being the height and depth of the 2D channel, adjusts the current per unit wire ds [m] to the current over the entire wire, with ds being oriented along the perimeter of the wire. Note that the integral is coordinate-adjusted for the open space configuration #3. The required electrical power is then straightforwardly obtained

$$P_{el} = I \bullet \phi_1 \quad (10)$$

For the airflow rates \dot{V} [$\text{m}^3 \text{s}^{-1}$], we take the integral over the boundary, i.e., for the total flow rate, the integral over the channel outlet

$$\dot{V} = H \bullet \int_0^H \mathbf{u} dy \quad (11)$$

whereas the average velocity \bar{u} [m s^{-1}] expression is

$$\bar{u} = \frac{1}{H} \int_0^H \mathbf{u} ds \quad (12)$$

For the open space case, the flow-related integrals are taken 450 mm downstream from the electrode. Also, for the open space case, Equations 9–12 are formulated in terms of axisymmetric systems. Another

important metric is the amplification factor, simply the ratio between EHD-generated and amplified airstream.

$$AF = \frac{\int_{Outlet} \mathbf{u} ds}{\int_{Inlet} \mathbf{u} ds} \quad (13)$$

Lastly, as a measure of efficiency, we use the transduction efficiency (Wang et al., 2013), i.e., the flow rate per electrical power γ [$\text{m}^3 \text{h}^{-1} \text{W}^{-1}$],

$$\gamma = \frac{\dot{V}}{P_{el}} \quad (14)$$

Typically, the efficiency of fans is determined with fan pressure and flow rate as performance parameters (Onma and Chantramsi, 2018). However, our EHD air amplification configurations operate at atmospheric conditions with little pressure rise of a few Pascal. Therefore the transduction efficiency proves useful to compare EHD-based devices to conventional airflow generation devices, particularly in application areas where the focus is on generating localized airflow, such as in food drying (Onwude et al., 2021), (Defraeye and Martynenko, 2018b).

3. Results

3.1. Proof-of-concept constrained flow EHD air amplification

3.1.1. Fan pressure curve for EHD air amplifier configuration #2

This section presents the pressure–flow rate curve of our conceptual EHD air amplification configuration #2. The simulation result for velocity magnitude is shown in Fig. 6, featuring the best-performing set of parameters in terms of airflow. The pressure–flow rate curve is calculated by choking the flow via a damping screen miming an orifice plate.

The resulting fan pressure curve of the EHD air amplifier is given in Fig. 7. EHD air amplifiers can generate a pressure lift of a few Pascal at the highest parameter setting. This result is expected, as similar pressure rise level have been reported for ionic wind-driven flows (Jewell-Larsen et al., 2011). EHD air amplifiers might not be a suitable replacement for conventional axial fan applications that meet a considerable pressure resistance. Nevertheless, EHD air amplifiers may provide a valuable alternative for air circulation and ventilation at near-atmospheric pressure conditions, especially indoors.

Fan pressure curves are an essential design instrument for conventional applications. However, in the case of EHD air amplifiers, we will focus on high-volume low-pressure applications for which the transduction efficiency (flow rate per electric power) and the amplification factor (outflow per inflow) provide more practical evaluation and design metrics.

3.1.2. Air amplifier vane aerodynamic performance with and without EHD

This section aims to understand the aerodynamic performance of the

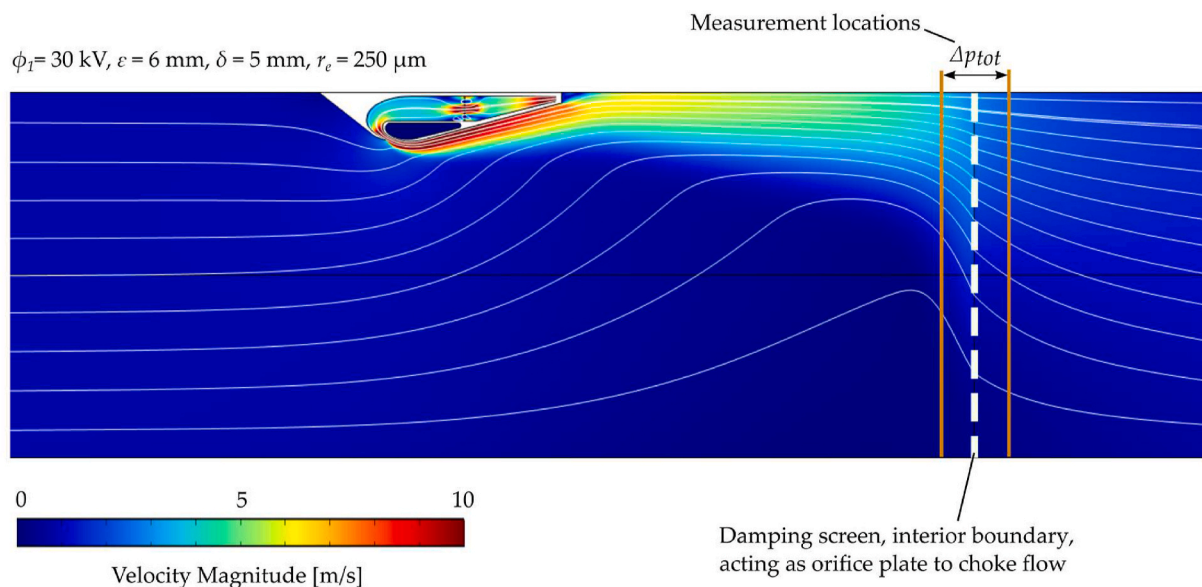


Fig. 6. Velocity field of the modified setup of configuration #2. An interior boundary with variable porosity represents the equivalent of an orifice plate to enable flow choking. Before and after the interior boundary, the pressure and velocity are measured to calculate the total pressure difference.

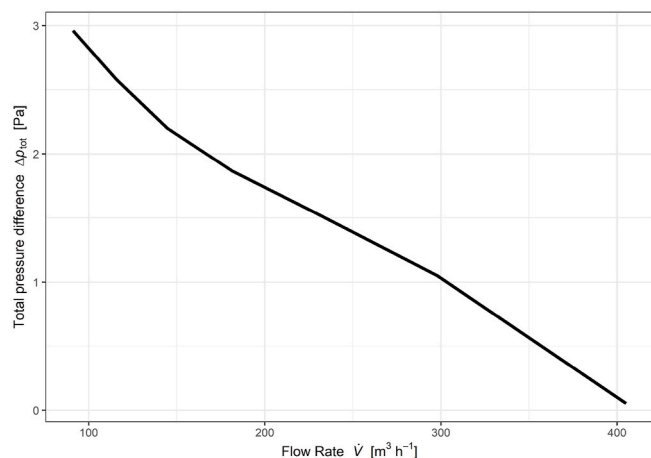


Fig. 7. Fan pressure curve of the EHD air amplifier as in configuration #2.

vane as in configuration #2, first without and then with EHD. We do this by showing the supply pressure-flow rate characteristic to assess which flow rates correspond to how much electrical power is input. In this CFD-only simulation, the supply pressure is understood as the pressure a compressor would have to deliver to the core of the vane. In Fig. 8, the curve shows the performance of this particular geometry in standard settings. We obtain the vane air amplifier curve without EHD by simulating CFD-only mode with an imposed velocity inlet within the vane. When operating the vane with EHD airflow generation, we can achieve a maximal airflow rate for the current vane, as otherwise, breakdown occurs. The shaded area shows values obtained from EHD air amplification simulations at the closest electrode distance $\delta = 5$ mm, since it provides the strongest flow rates, see also Fig. 11b. Moreover, the electric power demand lines are plotted for a given flow rate. In the simulations, the highest achieved airflow rate is $\dot{V} = 407 \frac{m^3}{h}$ for the enclosed EHD air amplifier configuration #2. For such a flow rate, an electric power of 470 W is predicted by the simulations. In practice, this value is too high for corona discharge, and a spark would form instead of a continuous discharge. Sparks are highly non-linear phenomena that are not included in our model due to complexity reasons. We keep the high power prediction here for theoretical reasons. However, with

another discharge principle, dielectric barrier discharge (DBD), higher power levels are achievable also in practice, but this is beyond the scope of this study.

An electrical power input for EHD airflow of 10 W is more realistic. It is clear that with 10 W, flow rates of less than $100 \frac{m^3}{h}$ with little supply pressure can be achieved. Hence, the chosen configuration for constrained flow EHD air amplification is probably preferred for high-pressure applications.

3.1.3. Impact of geometrical parameters on EHD air amplification performance

In this section, we describe how geometrical parameters affect the air amplification performance of the EHD-equipped vane. The geometrical parameters are the size of the vane nozzle gap ϵ and the height of the channel H as flow confinement parameters of the EHD air amplification confined space configuration #2. Also, we include the radius of the electrode r_e as a geometrical parameter impacting both the fluid flow and electrical performance. We evaluate the volume flow rate at the end of the channel and transduction efficiency in terms of flow rate per electrical power at the basecase voltage $\phi_1 = 15$ kV and an inter-electrode distance $\delta = 10$ mm. Fig. 9 summarizes the flow rate and transduction efficiency results under the described geometrical parameters. Note that the dashed line represents each parameter's arbitrarily chosen basecase value.

The most prominent finding is that there appears to be an optimum for the nozzle gap at $\epsilon = 6$ mm. We obtain both maximum transduction efficiency and volume flow rate, as seen in Fig. 9a–d. A too-large nozzle gap ($\epsilon = 10$ mm) creates a flow separation zone that leads to flow detachment and impedes the formation of the Coanda effect. The flow detachment is also shown in Fig. 10b. A too-narrow gap ($\epsilon = 1$ mm) seems to pose an important flow resistance that weakens the EHD-generated airstream and ultimately weakens the more significant, amplified bulk flow within the channel. According to Fig. 9c–f, we observe the flow rates rise with the larger size of the flow confinement area when it comes to the impact of the channel height. With increasing channel size, air entrainment has a more significant effect due to the larger volume of air available. The same applies to the electrical power invested, which remains constant, and therefore more flow contributes to an overall transduction efficiency gain. The results indicate an opposite behavior in maxima and minima for the wire radius. The volume flow rate is at its maximum for the smallest dimension, $r_e = 50 \mu m$,

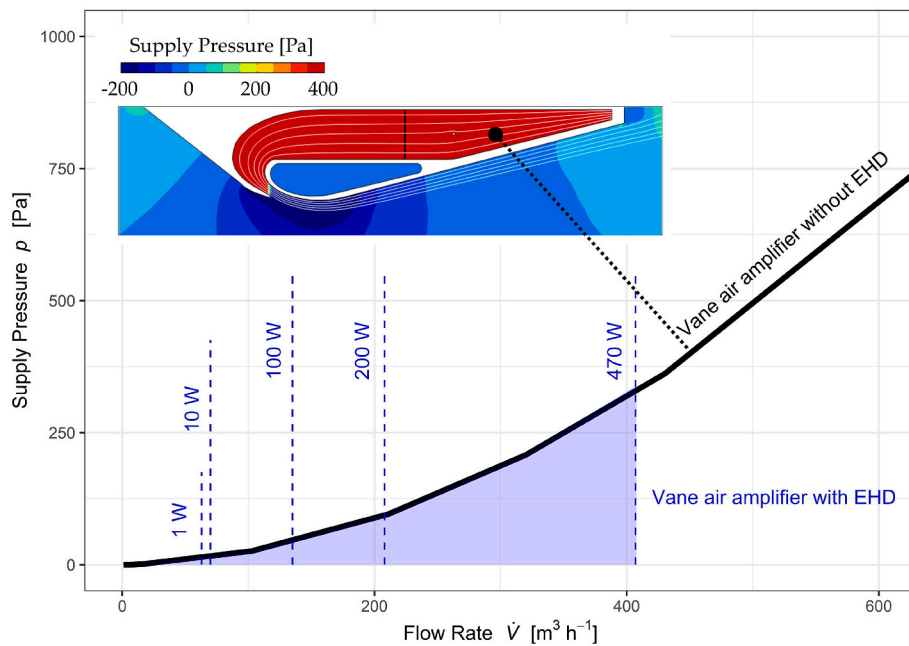


Fig. 8. Supply pressure and flow rate characteristics of configuration #2 with vane enclosure. The supply pressure is the pressure that an air compressor laterally attached to the vane would need to deliver to the interior of the vane enclosure to achieve certain flow rates at the outlet of the channel. The blue-shaded area illustrates the situation when the vane is powered by EHD instead of pressurized air. Typically, EHD operates with a power input of a few watts resulting in supply pressures of a few Pascal. We can calculate powers up to 470 W in-silico, but in practice, this value would not be achievable for this configuration due to the risk of arc discharge and electrical breakdown. (For interpretation of the references to colour in this figure legend, the reader is referred to the Web version of this article.)

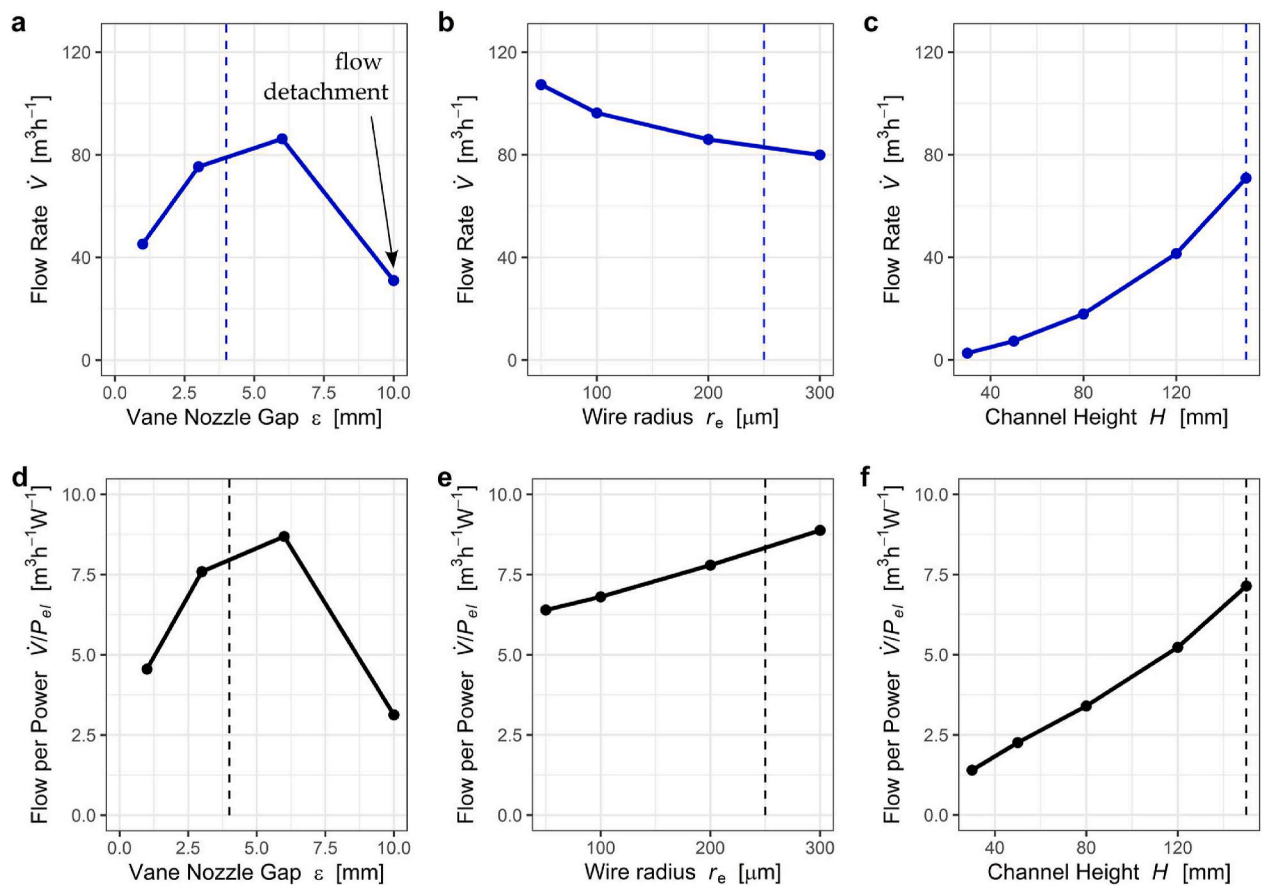


Fig. 9. Flow rate and transduction efficiency (flow per power) results for various geometrical parameters. (a) to (c) show the behavior of the channel bulk flow rate under the influence of vane nozzle gap, wire radius, and channel height. Graphs (d) to (f) show the impact on transduction efficiency. The dashed lines represent the standard base case settings for each corresponding parameter setting.

as seen in Fig. 9b. This is due to the stronger curvature of the wire, which yields a stronger electric field and, thus a more potent Coulomb force which translates into an increase in momentum transfer. Conversely, the

transduction efficiency curve in Fig. 9e demonstrates that larger wire diameters are beneficial for obtaining more flow for the same electrical power input. The wire radius poses a design challenge where a trade-off

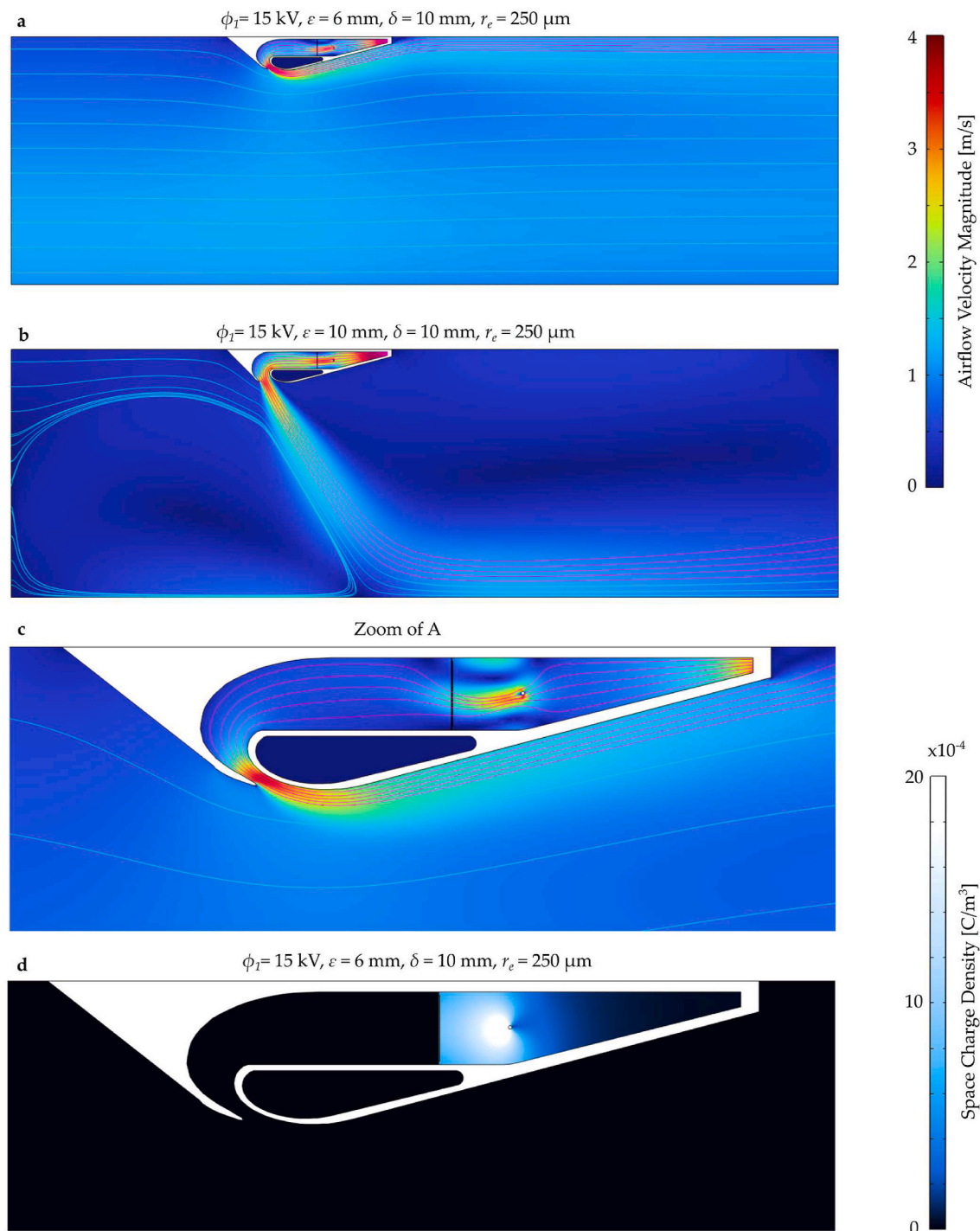


Fig. 10. Selected EHD air amplifier flow fields of configuration #2 for the flow field (a) to (c) and space charge density distribution (d). The EHD-generated flow is marked by magenta streamlines, while the amplified flow rate is cyan. Subfigures (a) and (b) differ in nozzle gap size, exemplarily showing that the flow detaches from the Coanda surface in the latter case. (For interpretation of the references to colour in this figure legend, the reader is referred to the Web version of this article.)

must be found.

In Fig. 10, flow fields and the space charge density field are shown for selected cases. The results depicted in Fig. 10a–c correspond to the optimum for the nozzle gap size $\varepsilon = 6$ mm where transduction efficiency and volume flow rate are expected to be highest. For this parameter selection, EHD air amplification operates as intended. The EHD-generated airstream remains attached to the Coanda surface of the vane enclosure and drags the air within the channel along.

In the following picture, Fig. 10b, we see a non-operational EHD air amplifier, which happens if the gap size is too large, i.e., $\varepsilon = 10$ mm and

above. Fig. 10b also explains the substantial decay in volume flow rate and transduction efficiency, as seen in Fig. 9a–d. Note that the gap size is too large for this configuration. The in-vane flow takes a 180-degree turn and, with a 10 mm gap, will just shoot to the bottom of the channel without attachment of the air jet due to the Coanda effect. It is indeed possible to create a geometry where the Coanda effect and flow attachment persists even with a gap size of $\varepsilon = 10$ mm or more. Such a geometry would for example be a nozzle that ends on a flat plate. So for this convex surface, there is an optimum gap size. However, the concept of EHD air amplification is strongly geometry-dependent such that a

general answer on the ideal nozzle size cannot be given.

Fig. 10d depicts the space charge density distribution, and it looks similar for all parameter variations of electric potential, vane nozzle gap size, and wire radius. What changes is mostly the intensity of the space charge density. We show the ionized, electrically conductive part of air with the space charge density distribution. It also represents the area where the Coulomb force acts on the air. The acceleration region can be seen, i.e., also in the velocity field in Fig. 10c. There is the inter-electrode space where the airflow experiences a strong acceleration. In fact, by integrating the electrodes within an enclosure such as a vane, in this case, practical applications can be targeted. In practice, high voltage components need to be shielded from the surroundings for safety reasons. Our simulations also show no more electrical charges downstream of the mesh ground, which means that we can assume the channel bulk flow to be charge-free. Charge-free flow is another advantage EHD air amplification has over regular EHD when safety issues are of concern.

3.1.4. Electrical and flow performance maps of regular EHD and EHD air amplification

As a result of the parametric studies of the configurations for EHD air amplification (#2, “amplifying”) and regular EHD (#1, “non-amplifying”), we show the performance maps in Fig. 11. The amplifying configuration #2 features the vane enclosure where the electric potential varies from 10 to 30 kV. Also, the electrode distance is varied between 5 and 25 mm. The same parametric study is duplicated for the regular EHD case #1 without air amplification. One of the most important results is the voltage-current relationship, as per Fig. 11a. Here, both configurations show similar behavior, with about 20% higher

current on behalf of the amplifying case, which means that the vane enclosure animates the wire to produce more charge. Note that the distance of the electrode has an essential impact on the corona discharge onset voltage. While at the smallest distance, $\delta = 5$ mm, we can produce EHD-flow at $\phi_1 = 10$ kV already, the onset for 25 mm distance occurs after 16 kV. Fig. 11b shows the volume flow rate at the channel’s outlet at various voltage levels. For the amplifying geometry, the flow rate encompasses the EHD-generated airstream plus the amplified airstream, while for the non-amplifying configuration, the flow chart is the EHD-generated airstream alone. The fields do not overlap. The non-amplifying case can provide higher flow rates up to more than 1000 $\text{m}^3 \text{h}^{-1}$ over the entire voltage operation range. Also, we can see that a closer electrode distance generates more substantial airflow rates.

So far, the non-amplifying benchmark case outperforms the EHD air amplification configuration in terms of lower electric current consumption and higher flow rate. However, after a specific voltage, $\phi_1 \sim 16$ kV, the EHD air amplifier configuration shows superior transduction efficiency, as seen in the flow rate per electrical power chart in Fig. 11c. For non-amplifying regular EHD, there is no electrode distance-dependent difference in the flow rate to electric power ratio. Moreover, at lower voltages, the non-amplifying case is up to three times more effective in generating a specific flow rate than the amplifying case. Afterward, the transduction efficiency rapidly decreases, and the EHD air amplification becomes more performant, given that the electrodes are distant enough. For close distance, $\delta = 5$ mm, regular EHD still prevails in transduction efficiency. For comparison, the red dashed line represents an ordinary compact DC axial fan of comparable size (Model 5318/2 TDHHP, 66 W, 490 $\text{m}^3 \text{h}^{-1}$, ebm-papst St. Georgen GmbH & Co.

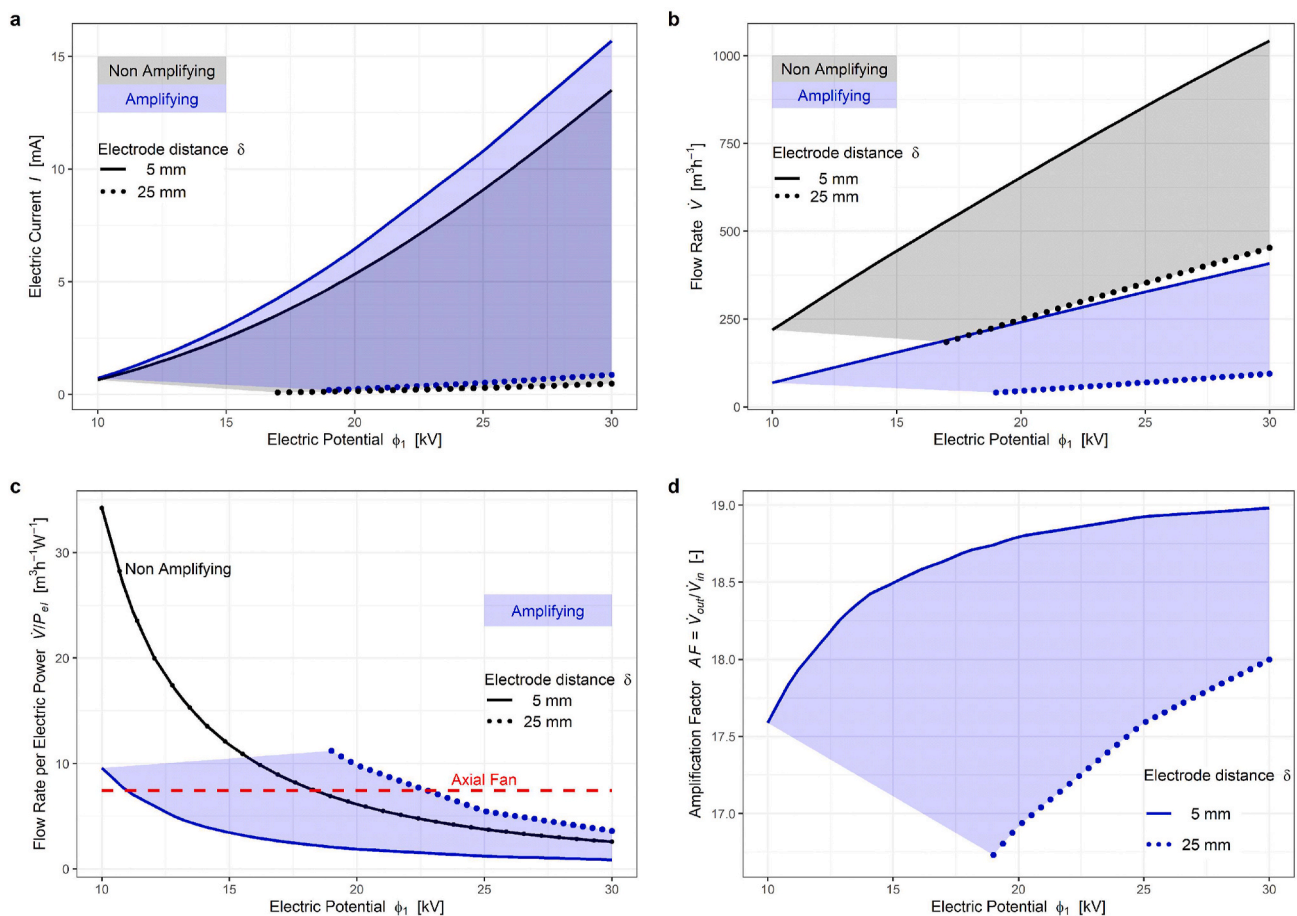


Fig. 11. Electrical and flow performance maps resulting from parametric studies of the amplifying (#2) and non-amplifying (#1, benchmark) configuration. Subfigures (a) and (b) directly compare the voltage-current relationship and the voltage-volume flow rate relationship. Subfigure (c) shows the flow rate to electric power ratio, including an ordinary axial fan, and (d) plots the amplification factor range.

KG). In the domain of airflow generation at atmospheric conditions, EHD air amplification appears competitive energy-wise with an increase in transduction efficiency of 34–48% (at 10–19 kV) compared to this selected regular fan.

The flow rate per electric power is calculated from the flow rate and electric current. The latter experiences a non-linear behavior that leads to plateauing at increased voltage levels. This is evidence that increasing the total charge volume in the drift region affects the Coulomb force, so

the momentum transfer to the air suffers.

Another metric for a flow rate increase is the amplification factor. The invested electric energy is, as a result of this, locked within the EHD-generated airstream equivalent to a flow rate of \dot{V}_m used for the Coanda effect. With this effect, a more significant bulk flow is induced with a flow rate \dot{V}_{out} . Fig. 11d shows the performance map of the amplification factor. The amplification factor ranges from 16.5 to 19, and the relative amount of airflow obtained is “for free” without costing further

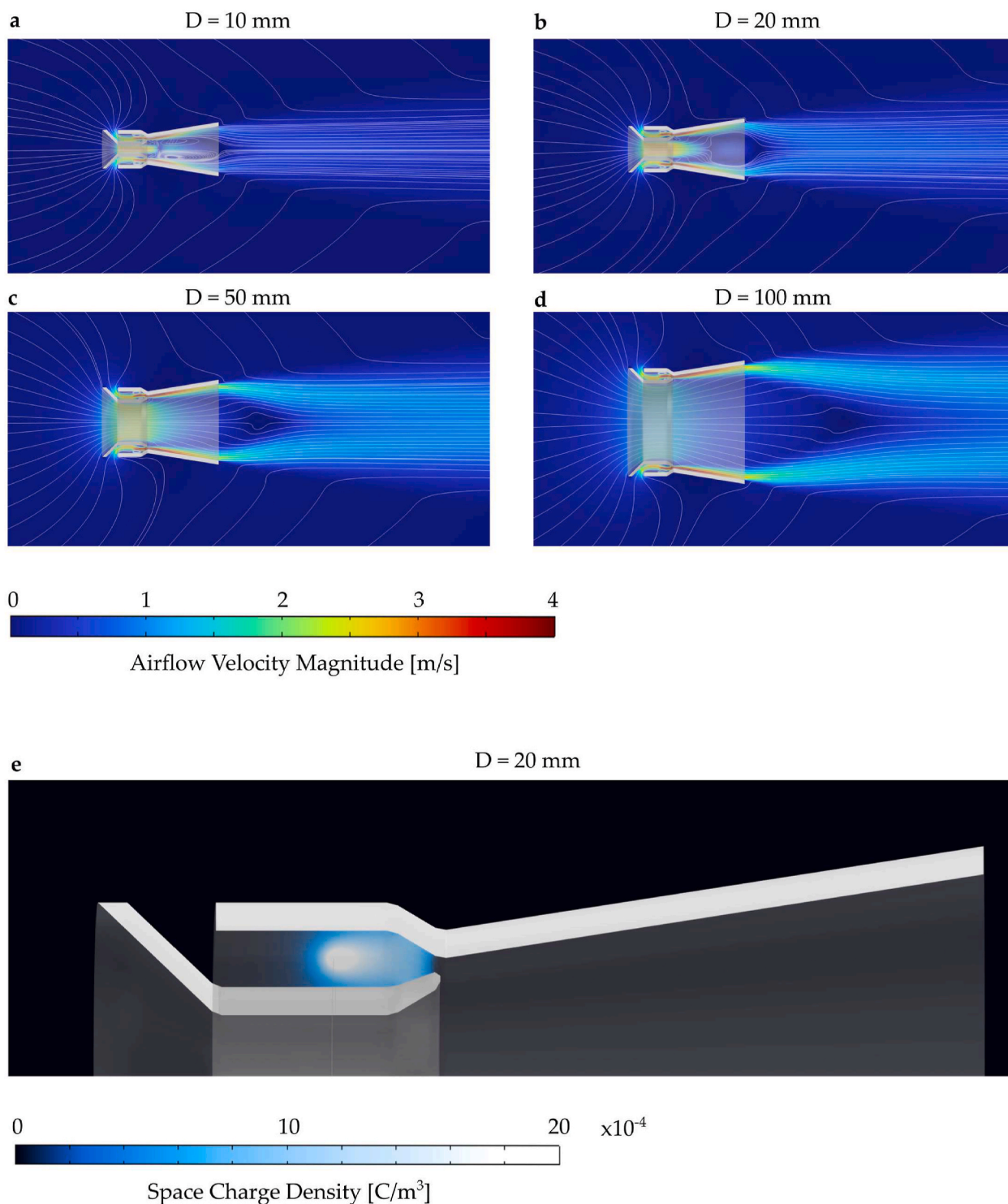


Fig. 12. Velocity fields for the 2D-axisymmetric case configuration #3. The various inner diameter dimensions are portrayed in Subfigure a-d. Subfigure E shows the space charge density distribution within the amplifying vane. In contrast to confined flow EHD air amplification, the open space configuration also shows that surrounding air is dragged additionally via entrainment.

electrical energy. In comparison, air amplifiers typically amplify the incoming airstream up to a factor of 15 (Air Technology Air Efficiency Range, Mansson and Traberg-Larsen, 2014). With the present EHD air amplifier numerical proof-of-concept in this work, a similar or even superior amplification factor completely bladeless can be achieved in a solid-state fashion.

3.2. Proof-of-concept open space EHD air amplification

3.2.1. Flow patterns of open space EHD air amplifiers

The open space EHD air amplifier construction consists of two independent components that overlap and form an enclosure. Inside, we accommodate the wire electrode and the ground electrode, embedded in both components' nozzle sections. In practice, the ground could be done via copper tape, while the two PLA components are 3D-printed. Note that in this EHD air amplifier design, we have a non-convex straight Coanda surface with an angle of 9.26° . The shape and dimensions of the vane are arbitrarily chosen and will be studied in more detail in future research. Here, we show that EHD air amplification also works in open spaces for various dimensions. Many air amplifiers are used in the free field. As a reminder, to achieve EHD air amplification, three elements are necessary, a high voltage electrode (wire, needle, or any other shape with sub-millimeter curvature), an air cavity where the electrodes are embedded inside, and a Coanda surface, i.e., a surface facilitating the Coanda effect with subsequent air entrainment.

Those three necessary elements are built into this open space EHD air amplifier. In Fig. 12a–d, there are cutouts of the larger flow field for different inner dimensions D while the other dimensions of the vane are kept constant. The EHD air amplifier takes surrounding air and forms an airstream jet. Downstream the airflow jet is where the total flow rate is measured. The total flow rate in open space consists of three connected airstreams: the EHD-generated airstream, the amplified airstream, and the entrained airstream. The latter is a collateral airstream dragged along the amplified airflow jet in the open space. We observe the entrained airstream in the plots as surrounding streamlines from the broader open space appear and accelerate in the propagation direction of the jet. Additionally, it is also noted that the size of the air amplifier has an impact on the evolution of the velocity between the inner Coanda surfaces. Smaller dimensions, such as 10 and 20 mm, as per Fig. 12a and b, form a type of recirculation zone, ultimately leading to a loss in transduction efficiency. Hence, the first results show that scalability is given. However, on a geometrical level, there is still space for streamlining, for example, by changing the angle of the Coanda surfaces or even curving them to form a convex shape.

Fig. 12e shows the distribution of space charge density within the enclosure, which is similar in all cases. In the confined space EHD air amplifier case, it was observed that the space charge does not penetrate the larger bulk flow. The same situation is also given in this 2D-axisymmetric design, where the grounded electrode is embedded into the nozzle. We must also acknowledge that it is a special air amplifier design. In reality, the air supply is not so close to the entrainment area.

3.2.2. Impact of EHD air amplifier scaling on performance characteristics

Amidst the many parameters that can be checked in EHD air amplification, for the open space case, we will focus on the inner diameter of the device only, as here we have the advantage of checking for scalability of the entrainment area of EHD air amplifiers. The goal is to achieve maximum flow rates. Hence the wire is set to $r_e = 50 \mu\text{m}$ based on the findings shown in Fig. 9b. The inter-electrode distance and gap size are kept as in the basecase simulation. The confined space EHD air amplifier vane and this discussed vane are only limitedly comparable for the electrode arrangement as the grounded electrode here is embedded within the nozzle. Also, the EHD-generated airstream does not reverse within the vane. Instead, it deviates up to a maximum clockwise angle of 90° . Hence, based on the previous calculations, only the information about the wire electrode radius is taken as a design

parameter to achieve maximum flow rates.

The results for the electrical and flow performance are shown in Fig. 13. With increasing inner diameter D from 10 to 100 mm, the circumference of the entire structure increases with it. The power consumption increases linearly, as seen in Fig. 13a. The volume flow rate exhibits similar behavior as per Fig. 13b, where the volume flow rate is measured at a distance of 350 mm from the vane. However, in terms of transduction efficiency, there appears to be an optimum of as per Fig. 13c. Here, an inner diameter of 50 mm performs about 10% better than the smallest case with an inner diameter of 10 mm. Compared to the aforementioned axial fan, this open space EHD air amplifier provides more flow rates per electrical power invested over the entire range of sizes. Also, the chosen benchmark axial fan has dimensions of 140×140 mm (Model 5318/2 TDHHP, 66 W, $490 \text{ m}^3 \text{ h}^{-1}$, ebm-papst St. Georgen GmbH & Co. KG). A solid-state and noiseless EHD air amplifier for downsized energy-efficient applications might be a worthwhile alternative to consider. Of course, in terms of flow rates, the axial fan still outperforms the EHD air amplifier by a factor of approximately 3.5 (when compared to the $D = 100$ mm setup). We also evaluate the amplification factor in Fig. 13c. The amplification factor is somewhat difficult to determine in an open space environment as the EHD-generated airstream is part of the larger volume before entering the amplifier. However, in the established numerical simulations, the EHD-generated airstream \dot{V}_{in} inside the vane can conveniently be retrieved by integration of the airflow velocity in that specific area. The results show that in open space, a considerably lower amplification factor, up to 6.4, is obtained than the constrained EHD air amplifier, which was up to 19.

4. Discussion

4.1. Numerical proof-of-concept of EHD air amplification

We demonstrated numerically the concept of a novel EHD air amplifier with the ambition to increase flow rates and improve the aerodynamic yield per Watt invested (transduction efficiency). The low flow rate problem is inherent with EHD. The key novelty is to combine EHD with the Coanda effect, which allows using the EHD-airstream as a bleed flow to induce a larger bulk flow, thus boosting the flow rate and overall transduction efficiency.

The vast design space of EHD air amplification is best explored with our fully-automated corona discharge numerical model. The numerical approach has been validated with experimental data (Jewell-Larsen et al., 2008) and also analytically verified in a test-case simulation detailed in Supplementary Material B (Rubinetti et al., 2015). We studied two types of EHD air amplifiers with this tool: a confined space configuration (#2) and an open space configuration (#3). The confined space configuration #2 has undergone extensive parametric runs. The goal of increasing EHD-generated flow rates has been met. Compared to regular EHD and a conventional axial fan, the conceptual EHD air amplification is able to generate more flow rates per electrical energy invested after a threshold voltage of 19 kV. The regular EHD benchmark still produces higher flow rates in the confined channel setup, albeit at higher electrical costs. For the open space case, configuration #3 shows that scalability is possible. Among the numerous study parameters, the geometry-relevant ones play a more significant role.

4.2. Applicability of EHD air amplification

EHD air amplification is a potential candidate for various ventilation and air circulation applications, both in industry and for domestic use. With the housing or enclosure an EHD air amplifier needs, we can separate the delicate high voltage components from the surroundings. We expect EHD air amplification technology to be adopted, e.g., in.

- Alternative fan devices with little to no pressure rise

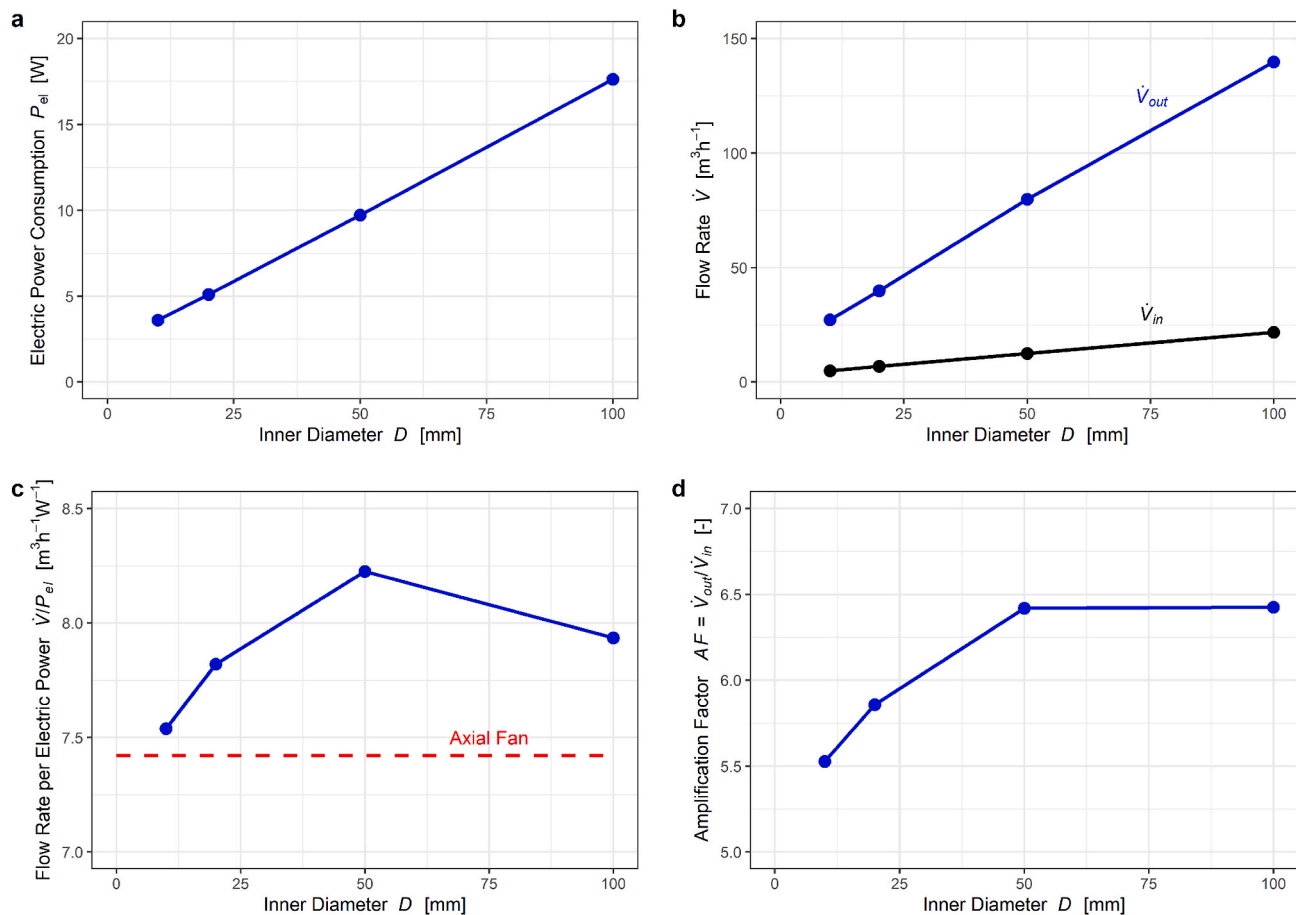


Fig. 13. Electrical, flow, and transduction efficiency results for the 2D-axisymmetric vane configuration #3 for various inner diameter dimensions. For comparison purposes, the transduction efficiency in flow rate per electric power also shows an ordinary axial fan.

- o Noiseless domestic fans
- o Ventilation
- o Air distribution
- o Air circulation
- Applications
 - o Cooling/heat dissipation
 - o Active flow control
 - o Surface drying
 - o Extraction of gases and small particles
 - o Decontamination/disinfection control

Disinfection control might be attractive to medical and food processing purposes as EHD air amplifiers produce ozone as a co-product. For domestic use, an EHD air amplifier must also remove or dilute the ozone to a sub-critical level. As such, EHD air amplifiers could serve, apart from airflow generation, also a decontamination function and even help in particle removal.

In general, EHD air amplifiers are, among other applications, suitable as components for improving the efficiency of a more extensive system that needs customized airflow distributions. The reason is that EHD air amplification cannot fully replace, e.g. axial fans, due to its limited pressure rise of 3 a few Pascal. As such, ionic wind-based devices are not an alternative airflow propulsion device, but they can be an auxiliary retrofit technology to locally produce airstreams to decrease the overall power consumption. For example, in the case of high-concentrating photovoltaics (Shao et al., 2022), a customized and locally produced airstream dissipates enough heat to reduce the cell temperature by more than 15 °C and improve its efficiency. The constructive benefit of EHD and EHD air amplification is that it can be operated in a decentralized

way which gives better control over airflow patterns. Indoor air quality is an increasingly important topic for air-tight buildings (González-Martín et al., 2021). EHD air amplifiers could help reduce the energy consumption of the central ventilation unit by assisting it in distributing the air within single room. Moreover, for drying applications, EHD air amplifiers can provide a suitable alternative to the current state of the art, which usually involves combining a fan with a heating coil. Providing targeted airflow can improve the convective aspect of such drying processes while omitting the energy-intensive heating component (Iranshahi et al., 2022).

4.3. Possible hurdles and limitations in practical implementation

Several aspects might pose problems when translating the numerical study into an experimental prototype. EHD air amplification with a wire was systematically assessed on a numerical level, and the numerical model could produce data for a wide operation range. However, in practice, such high voltages might result in sparkover, i.e., when the corona discharge is not continuous anymore and starts arching. The arching problem is also more present for wires in the presence of a dielectric such as the PLA enclosure since it has a higher permittivity or in environments with elevated humidity. A higher permittivity might distort the electric field in a way that makes it more homogeneous around the discharging electrode, and as such, the high gradients to sustain a continuous discharge are absent. Therefore, it is worth considering needle shapes or other sharply edged geometries as discharging electrodes for practical application.

Lastly, in particular parameter combinations, namely, when the voltage is high and the inter-electrode is close, several hundred Watts of

electrical power are obtained, meaning a great potential leading much higher flow rate. In practice, EHD operates at a few Watt electrical power. Although such a strong power can be realized in silico, there is a serious risk of arching in practice.

5. Conclusion

We investigated in-silico a novel type of airflow propulsion device, called EHD air amplifier, an ionic wind-based technology capable of delivering high flow rates with little pressure rise and little energy consumption. Two configurations of EHD air amplifiers have been designed, one for confined space (#2) and one for open space (#3). Another regular EHD configuration (#1) served as a benchmark. Several design space parameters have been explored with a Lagrange-multiplier modeling approach that allows fast and automatic calculation of single-species EHD-driven flows. We obtained extensive parametric results such as the volume flow rate, current-voltage relationships, transduction efficiency in terms of flow rate per power, and amplification factors for both EHD air amplifier configurations. The key findings are.

- The EHD air amplifier in constrained flow configuration #2 improves the transduction efficiency at a voltage of 19 kV from 6.87 to 10.98 ($\text{m}^3 \text{h}^{-1}/\text{W}$ (+59%). It remains more efficient in producing flow rates than regular EHD also at higher operational voltages. Compared to a similar-sized axial fan, the EHD air amplifier yields 48% more airflow. Hence, EHD air amplifiers produce flow rates more efficiently per Watt invested than regular EHD devices and axial fans.
- In constrained configuration #2, amplification factors of 16.5–19 are achieved. For open space configuration #3, the amplification factor ranges from 5.5 to 6.4. EHD air amplifiers achieve similar amplification factors to normal air amplifiers.
- The open space configuration #3 performs best energy-wise with an inner diameter of 50 mm, where the peak transduction efficiency of 8.24 ($\text{m}^3 \text{h}^{-1}/\text{W}$) is predicted. In terms of maximum flow rates, an inner diameter of 100 mm yields 137 $\text{m}^3 \text{h}^{-1}$. The product is scalable, and there is a sweet spot in transduction efficiency.
- EHD air amplifiers perform efficiently, however, the maximum pressure lift of a few Pascals limits the application spectrum to air ventilation and distribution at near-atmospheric conditions.

The obtained physics-based simulation study results demonstrate that EHD air amplification is a promising way to improve ionic wind's intrinsically low airflow rates. By air amplification, we can increase the airflow rates of EHD with a factor of 19 in constrained flow and with a factor of 6.4 in open space. Also, the model developed in this study allows for fast computation of EHD-driven flows, which gives valuable insight into the design of EHD air amplifiers and EHD technology in general. Potential application fields for this technology are air distribution and circulation with little pressure rise.

CRedit authorship contribution statement

Donato Rubinetti: Conceptualization, Methodology, Investigation, Project administration, Writing – review & editing. **Kamran Iranshahi:** Methodology, Writing – review & editing. **Daniel Onwude:** Writing – review & editing. **Lei Xie:** Methodology, Writing – review & editing. **Bart Nicolai:** Writing – review & editing. **Thijs Defraeye:** Conceptualization, Methodology, Supervision, Funding acquisition, Project administration, Writing – review & editing.

Declaration of competing interest

The authors declare that they have no known competing financial interests or personal relationships that could have appeared to influence the work reported in this paper.

Data availability

Data will be made available on request.

Acknowledgments

The authors are grateful to the Swiss Innovation Agency (Innosuisse 34549.1 IP-LS) and Belimed AG for the financial support provided during project conceptualization and execution. This manuscript has been released as a preprint on engrXiv.

Appendix A. Supplementary data

Supplementary data to this article can be found online at <https://doi.org/10.1016/j.jclepro.2023.136531>.

References

- Air technology air efficiency range. Nov. 10, 2021. [Online]. Available: www.meech.com.
- Ambaw, A., et al., 2014. CFD-based analysis of 1-MCP distribution in commercial cool store rooms: porous medium model application. *Food Bioprocess Technol.* 7 (7), 1903–1916. <https://doi.org/10.1007/S11947-013-1190-9/FIGURES/16>.
- Behzadnezhad, B., Collick, B.D., Behdad, N., McMillan, A.B., 2018. Dielectric properties of 3D-printed materials for anatomy specific 3D-printed MRI coils. *J. Magn. Reson.* 289, 113. <https://doi.org/10.1016/J.JMR.2018.02.013>.
- Chua, K.J., Chou, S.K., Yang, W.M., Yan, J., 2013. Achieving better energy-efficient air conditioning – a review of technologies and strategies. *Appl. Energy* 104, 87–104. <https://doi.org/10.1016/J.APENERGY.2012.10.037>.
- Defraeye, T., Martynenko, A., 2018a. Electrohydrodynamic drying of food: new insights from conjugate modeling. *J. Clean. Prod.* 198, 269–284. <https://doi.org/10.1016/j.jclepro.2018.06.250>.
- Defraeye, T., Martynenko, A., 2018b. Electrohydrodynamic drying of food: new insights from conjugate modeling. *J. Clean. Prod.* 198, 269–284. <https://doi.org/10.1016/j.jclepro.2018.06.250>.
- Diffuser, Buice. Jan. 13, 2023). <https://www.grc.nasa.gov/WWW/wind/valid/buice/buice.html>.
- Dumitrache, A., Frunzulica, F., Ionescu, T.C., 2012. Mathematical modelling and numerical investigations on the Coanda effect. In: *Nonlinearity, Bifurcation and Chaos - Theory and Applications*. InTech.
- Gammack, P.D., Nicolas, F., Simmonds, K.J., 2012. FAN," *US* 8 (445 B2), 308.
- González-Martín, J., Kraakman, N.J.R., Pérez, C., Lebrero, R., Muñoz, R., 2021. A state-of-the-art review on indoor air pollution and strategies for indoor air pollution control. *Chemosphere* 262, 128376. <https://doi.org/10.1016/J.CHEMOSPHERE.2020.128376>.
- Guan, Y., Vaddi, R.S., Aliseda, A., Novosselov, I., 2018. Analytical model of electrohydrodynamic flow in corona discharge. *Phys. Plasmas* 25 (8). <https://doi.org/10.1063/1.5029403>.
- K. Iranshahi, D. I. Onwude, D. Rubinetti, A. Martynenko, and T. Defraeye, 2022 "Scalable Electrohydrodynamic Drying Configuration for Dehydrating Biological Materials at Industrial Scale," doi: 10.31224/2328.
- Iranshahi, K., Martynenko, A., Defraeye, T., 2020. Cutting-down the energy consumption of electrohydrodynamic drying by optimizing mesh collector electrode. *Energy* 208, 118168. <https://doi.org/10.1016/j.energy.2020.118168>.
- Jewell-Larsen, N.E., V Karpov, S., Krichtafovitch, I.A., Jayanty, V., Hsu, C.-P., V Mamishev, A., 2008. Modeling of corona-induced electrohydrodynamic flow with COMSOL multiphysics. *Proc. ESA Annu. Meet. Electrostat.* (–13), 1.
- Jewell-Larsen, N.E., Joseph, G.G., Honer, K.A., 2011. Scaling laws for electrohydrodynamic air movers. <https://doi.org/10.1115/ajtec2011-44626>.
- Johnson, M.J., Tirumala, R., Go, D.B., 2015. Analysis of geometric scaling of miniature, multi-electrode assisted corona discharges for ionic wind generation. *J. Electrostat.* 74, 8–14. <https://doi.org/10.1016/J.ELSTAT.2014.12.001>.
- Kanazawa, S., Imagawa, W., Matsunari, S., Akamine, S., Ichiki, R., Kanazawa, K. Ionic wind devices prepared by a 3D printer. Oct. 14, 2021. [Online]. Available: <https://ijpest.securesite.jp/Contents/11/1/PDF/11-01-038.pdf>.
- Kasdi, A., 2019. Experimental and Numerical Modeling of Corona Discharge Generated in an Electrostatic Precipitator. <https://doi.org/10.1109/CISTEM.2018.8613435>.
- Mansson, L.C., Traberg-Larsen, S.H., 2014. Flow characteristics of the dyson air multiplier. *Comput. Fluid Dyn. using Ansys Fluent* 14.5.7, 1–7.
- Onma, P., Chantrasmri, T., 2018. Comparison of two methods to determine fan performance curves using computational fluid dynamics. *IOP Conf. Ser. Mater. Sci. Eng.* 297 (1) <https://doi.org/10.1088/1757-899X/297/1/012026>, 012026.
- Onwude, D.I., Iranshahi, K., Rubinetti, D., Martynenko, A., Defraeye, T., 2021. Scaling-up electrohydrodynamic drying for energy-efficient food drying via physics-based simulations. *J. Clean. Prod.* 329, 129690 <https://doi.org/10.1016/J.JCLEPRO.2021.129690>.
- Panitz, T., Wasan, D.T., 1972. Flow attachment to solid surfaces: the Coanda effect. *AIChE J.* 18 (1), 51–57. <https://doi.org/10.1002/aic.690180111>.
- Ramadhan, A.A., Kapur, N., Summers, J.L., Thompson, H.M., 2017. Numerical modelling of electrohydrodynamic airflow induced in a wire-to-grid channel. *J. Electrostat.* 87, 123–139. <https://doi.org/10.1016/j.elstat.2017.04.004>.

- Rickard, M., Dunn-Rankin, D., Weinberg, F., Carleton, F., 2006. Maximizing ion-driven gas flows. *J. Electrostat.* 64 (6), 368–376. <https://doi.org/10.1016/j.elstat.2005.09.005>.
- Rubinetti, D., Weiss, D.A., Egli, W., 2015. Electrostatic precipitators-modelling and analytical verification concept. In: 2015 COMSOL Conf. Grenoble, pp. 14–16 [Online]. Available: https://www.comsol.com/paper/download/291561/rubinetti_paper.pdf <https://www.comsol.com/paper/electrostatic-precipitators-modelling-and-analytical-verification-concept-25951>.
- Shao, Z., Wang, B., Cai, L., Chang, C., Sun, L., 2022. Optical and thermal performance of dynamic concentrating solar module for building integration. *J. Clean. Prod.* 367, 132931 <https://doi.org/10.1016/J.JCLEPRO.2022.132931>.
- Taghian Dinani, S., Havet, M., 2015. The influence of voltage and air flow velocity of combined convective-electrohydrodynamic drying system on the kinetics and energy consumption of mushroom slices. *J. Clean. Prod.* 95, 203–211. <https://doi.org/10.1016/J.JCLEPRO.2015.02.033>.
- Tirumala, R., Go, D.B., 2011. Multi-electrode assisted corona discharge for electrohydrodynamic flow generation in narrow channels. *IEEE Trans. Dielectr. Electr. Insul.* 18 (6), 1854–1863, Dec. <https://doi.org/10.1109/TDEI.2011.6118623>.
- Wang, H.C., Jewell-Larsen, N.E., Mamishev, A.V., 2013. Thermal management of microelectronics with electrostatic fluid accelerators. *Appl. Therm. Eng.* 51 (1–2), 190–211. <https://doi.org/10.1016/j.applthermaleng.2012.08.068>. Pergamon.
- Wang, J., Jun Liu, Y., Zhu, T., Qiang Chen, Y., Bo Wang, J., 2021. Magnetic field enhanced ionic wind for environment-friendly improvement and thermal management application. *Appl. Therm. Eng.* 194, 117054 <https://doi.org/10.1016/j.applthermaleng.2021.117054>.
- Wu, Y., et al., 2017. Greener corona discharge for enhanced wind generation with a simple dip-coated carbon nanotube decoration. *J. Phys. D Appl. Phys.* 50 (39), 395304 <https://doi.org/10.1088/1361-6463/AA81A9>.
- Zhang, X., Li, H., 2020. Feasibility analysis for control of bioaerosol concentration at indoor corner via airflow from ventilation outlet with energy optimization. *J. Clean. Prod.* 248 <https://doi.org/10.1016/J.JCLEPRO.2019.119289>.
- Zhang, G.-W., Yang, J.-K., 2021. A review on recent advances and challenges of ionic wind produced by corona discharges with practical applications You may also like Numerical simulation on ionic wind in circular channels. *J. Phys. D Appl. Phys. Top. Rev.* 55, 153002 <https://doi.org/10.1088/1361-6463/ac3e2c>.
- Zhou, D., Tang, J., Kang, P., Wei, L., Zhang, C., 2018. Effects of magnetic field intensity on ionic wind characteristics. *J. Electrostat.* 96, 99–103. <https://doi.org/10.1016/J.ELSTAT.2018.10.007>.